J Mater Sci: Mater Med (2008) 19:2933–2940
DOI 10.1007/s10856-008-3424-3

Self-assembly of nanohydroxyapatite in mesoporous silica

Xuetao Shi · Yingjun Wang · Kun Wei · Li Ren · Chen Lai

Received: 20 October 2007 / Accepted: 29 February 2008 / Published online: 25 March 2008

Abstract A novel material hexagonal mesoporous silica-hydroxyapatite (HMS-HA) has been developed based on self-assembly of nanohydroxyapatite in mesoporous silica in situ. The structural and textural properties of the materials are, respectively, characterized via X-ray diffraction (XRD), Fourier transform infrared spectroscopy (FTIR), N_2 adsorption, thermogravimetic analysis, and high-resolution transmission electron spectroscopy (HRTEM). Variable crystallinity of HA involved in the mesopores yields from different sintering temperature, and correspondingly determines different degradation manners. This biocompatible new material hybridized nanoporosity to well acknowledge biofunctional scaffold (HA). It promises a high potential for application in drug and gene delivery.

1 Introduction

Hydroxyapatite (HA) inherently possesses high composition and structure similarities to the minerals found in native bones or dentin; therefore, it has been widely adopted as scaffold materials for bone tissue engineering making use of its bioactivity, biocompatibility, osteoconductivity, and noninflammatory behavior [1–3]. In addition, particles and porous granules of HA have also been investigated as carriers for various drugs, such as antibiotics and growth factors [4, 5].

Silicon is a common element in bioactive ceramics. It is reported that silicon plays an important role in connective tissue metabolism. Carlisle et al. demonstrated that fetal chickens fed with silicon-deficient diets showed significant disorder and retardation in growth and development [6, 7]. Silicon-substituted hydroxyapatite has been used as a novel bone regenerative material [7, 8]. α-$CaSiO_3$ ceramics, which are prepared via a coprecipitating process with NaOH, have also been developed as competent biomaterials with significant talent inducing HAP fast precipitation on simulated body fluid (SBF) [9, 10]. Bioactive glass (BG), developed by Hench and his colleagues in 1969, can bond directly with bone and soft tissues such as muscle [11–13].

Mesoporous silica materials possess a highly regular porous structure with uniform pore size, vast surface areas, and superior thermal stability, which makes them suitable for a variety of applications, particularly in the fields of catalysis [14–16] and separation [17], etc. Recently, several reports indicate that mesoporous silica also has great potential for applications in life sciences such as the carriers for drug and gene delivery [18–21]. Several general methods have been developed accordingly [22]. Methodological avenues have been opened, respectively, via electrostatic charge matching, hydrogen bonding, and dative bonding interactions between the interface of the micelles assemblies and silicate oligomer species. Hexagonal mesoporous silica (HMS) is a typical mesoporous molecular sieve that is produced via a neutral templating route. In comparison with MCM-41 family mesoporous materials, HMS possesses larger wall thickness, small scattering domain size, and complementary textural

X. Shi · Y. Wang (✉) · K. Wei · L. Ren · C. Lai
School of Materials Science and Engineering, South China University of Technology, Guangzhou 510641, China
e-mail: imwangyj@scut.edu.cn

X. Shi · Y. Wang · K. Wei · L. Ren · C. Lai
Key Laboratory of Specially Functional Materials and Advanced Manufacturing Technology, South China University of Technology, Ministry of Education, Guangzhou 510641, China
e-mail: PG23273810@ntu.edu.sg

mesoporosity; and additionally, their thermal and hydrothermal stabilities have also been remarkably improved. Moreover, for the removal of surfactants, HMS is free of high-temperature sintering, as the incorporation between surfactant and precursors during synthesis is barely based on hydrogen bonds [23, 24]. HMS provides a large, open and repeating structure on the nanometer scale. These special properties make it accessible to embed other nanoscaled functional materials such as hydroxyapatite and TCP into the mesopores.

In summary, two categories of inorganic carrier have been recently used for drug and gene delivery. They are, respectively, bioactive powders, such as calcium phosphate cements [25], hydroxyapatite [26], bioactive glass [27], and mesoporous silica, such as MCM-41 [28] and SBA-15 [29]. These two kinds of materials both have the pros and cons of their own: mesoporous silica provides vast surface area but lacks bioactivity; while the bioactive powders act invertly. Andersson et al. [30] have attempted to develop composites of apatite in mesoporous substrates, in which the apatite within the material has high crystallinity. In this study, we are interested in developing a new double-duty mesoporous material for controlled release and bone repair. This newly developed material (HMS-HA) not only inherits high surface areas made by nanopores from HMS, but also renders good bioactivity and biocompatibility from both HA and silica. We employed two simple methods to make hydroxyapatite nanoparticles self-assemble into the pores of mesoporous silica materials in situ, and then analyzed the synthesis scheme of HMS-HA mesoporous material as well.

2 Materials and methods

2.1 Materials

Tetraethyl orthosilicate (TEOS), ethyl alcohol (EtOH), $Ca(NO_3)_2$, $(NH_4)_2HPO_4$ were purchased from Chemical Reagent Factory (Guangzhou, China). Dodecylamine (DDA) was supplied by SSS reagent co., Ltd (Shanghai, China).

2.2 Synthesis methods

The synthesis of the material has been carried out via following two methods.

2.2.1 Method 1

HMS was synthesized via typical S^oI^o assembly as the reference [24]. TEOS was added to a vigorously stirred solution of DDA in ethanol and deionized water, affording a reaction mixture of the following molar composition: 1.0 TEOS\0.27 DDA\9.09 EtOH\29.6 H_2O. The reaction mixture was aged at ambient temperature for 18 h, and template removal was performed via extraction in hot EtOH of 45 and 80°C for 1 h, respectively. Then the product was dried in the oven at 90°C for 1 h.

After the dried process, the product was added into a mixed solution of $Ca(NO_3)_2$, $(NH_4)_2HPO_4$ and NH_4OH at a pH = 9 under continuous stirring for 2 h and then aged 24 h before calcined at 650°C for 9 h. The white powder achieved by calcined denoted as HMS-HA-EC1.

2.2.2 Method 2

DDA was used as a template, it was dissolved in an EtOH/deionized water solution containing $Ca(NO_3)_2$, $(NH_4)_2HPO_4$ and NH_4OH at a pH = 9. TEOS was used as the silica source. The mixture was stirring for 1 h and then aged for 18 h at ambient temperature. The product was dried in an oven at 90°C. Removing the template of the product was via three routes: (1) EtOH extraction; (2) EtOH extraction and calcination; (3) direct calcinations. The white powder products of the routes denoted as HMS-EE, HMS-HA-EC and HMS-HA-C.

2.3 Characterization

X-ray diffraction (XRD) analysis was performed on an X-ray diffractometer (XRD) (X Pert'PRO, PANalytical, The Netherlands) using a flat camera and 40 keV Cu-kα ($\lambda = 0.15418$ nm) radiation. The samples were scanned from 1° to 10° and 10° to 90° with a scan speed of 2°/min and 10°/min, respectively. Infrared spectra were recorded on a Nicolet Nexus 670 FT-IR spectrometer, and the samples to be measured were grounded with KBr and pressed into thin wafers. TGA-DSC was carried out on a NETZXSCH STA 449C thermal analyzer with the speed of heating as 10°C min^{-1} and the temperature ranging from 30 to 800°C under nitrogen atmosphere. Scanning electron microscopy (SEM) (30XLFEG, Philips, The Netherlands) was used to observe the morphology of hydroxyapatite and mesoporous particles. The samples were sputter coated with a layer of gold for observation at 10 kV. The morphology of material as-synthesize were dispersed in ethanol and characterized by HRTEM (JEM-2010, JEOL, Japan), using an accelerating voltage of 200 kV.

2.4 Weight loss

To evaluate the in vitro degradation of HMS-HA composite, discs of each sample (0.5 g, diameter 10 mm) were immersed in deionized water. The samples were stored at 37°C. At each time point, four samples of each formulation

were removed from the buffer and weighed after drying for 1 day. Four samples of each composition were measured and the results averaged. All measurements were expressed as an average ± the standard deviation.

3 Result and discussion

3.1 X-ray diffraction and BET analysis

The crystalline structure of the white powdery products was characterized by the powder X-ray diffraction (XRD) technique. As shown in Fig. 1, the SAXS pattern of all the HMS-HA exhibits single d (100) reflection as the typical HMS system mesoporous materials. The d (100) spacing was 43.1, 20.9, 38.7 Å for samples HMS-HA-EC1, HMS-HA-EC2, HMS-HA-C, respectively. The peak of d (100) reflections for all the samples were not very sharp and the intensity was feeble compared with traditional MCM-41 system mesoporous silica materials, which suggested that their formation was controlled by weak hydrogen bonding or other nonionic interactions. The intensity of the d (100) reflection of the ethanol-extracted HMS-HA-EC was more than three times that of calcined HMS-HA-C. This probably attribute to the extraction process which made HMS-HA form a kind of more completely cross-linked framework and prevented the structural collapse during the heating process [24]. By comparing the intensity of the peaks of HMS-HA materials fabricated by two methods, method 2 could yield a better long-range order structure.

The powder X-ray diffraction patterns of the HMS-HA-EE and HMS-HA-EC materials were identical to the standard cards (JPDS no. 9-432 for HA) according to the reflection peak positions and relative intensities that testified the identities of the products: hydroxyapatite crystals (hexagonal phase, space group $P6_3/m$). The amorphorous nature of the HMS of both samples and HA particles in HMS-HA-EE were confirmed by power X-ray diffraction in Fig. 2. There were no discerning diffraction peaks, but some broad humps at 22°, 31.8°, and 39.8°, which are characteristic of amorphorous phases. HMS-HA-EC, having been sintered at 250 and 650°C, and the peaks at 31.8°, 39.8° became sharp, whereas the hump at 22° were still existed. It was because that with the increase of temperature, the crystallinity of hydroxyapatite combined into the mesopores increased. However, mesoporous silica still kept the amorphorous condition. So, it was concluded that the broad humps at 31.8°, 39.8° were attributed to amorphorous hydroxyapatite in HMS; the hump at 22° corresponded to amorphous silicon. The fraction of crystalline phase (Xc) for the A crystal in mesopores could be evaluated by the following equation:

$$Xc = 1 - (V_{211/300}/I_{300})$$

where I_{300} is the intensity of (300) diffraction peak, and $V_{211/300}$ is the intensity of the hollow between (211) and (300) diffraction peaks of HA [31]. The evaluated degrees of crystallinity for HMS-HA-EC (sinter at 250°C) and HMS-HA-EC (sinter at 650°C) were 40 and 22%, respectively.

Surface areas and pore diameter distribution were revealed via N_2 adsorption–desorption isotherms and BJH pore size distribution curves for HMS-HA-EC (Fig. 3), the surface areas of HMS-HA between 300 and 500 m^2/g, which has smaller surface areas than traditional HMS materials (more than 1,000 m^2/g) [24]. And the pore size of HMS-HA (3.3 nm) was larger than HMS (2.4 nm) [24].

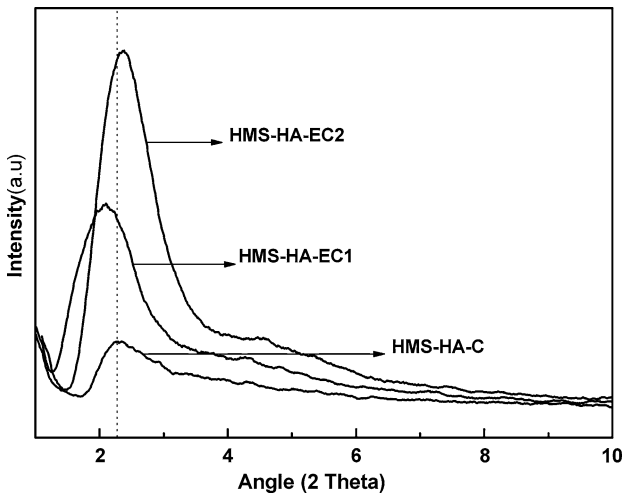

Fig. 1 SXRD pattern for HMS and HMS-HA materials with different synthesis methods (HMS-HA-EC1 was fabricated by method 1, and HMS-HA-EC2 was produced by method 2)

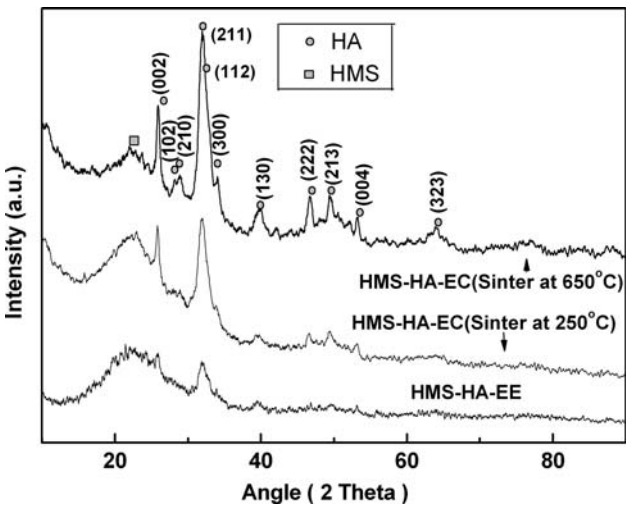

Fig. 2 WXRD pattern for HMS and HMS-HA materials with different synthesis methods and sinter temperature

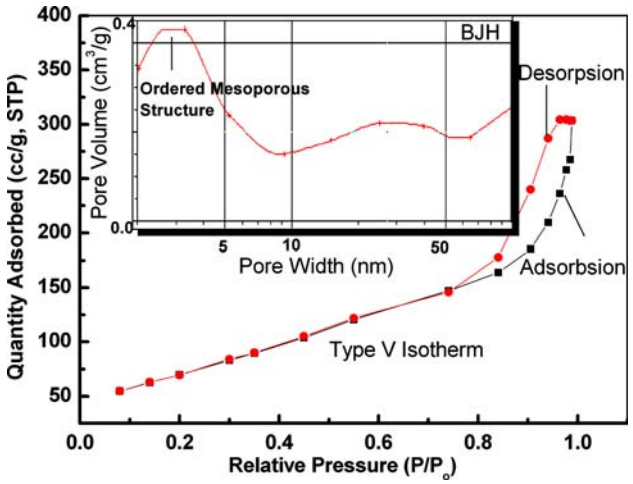

Fig. 3 Nitrogen adsorption and desorption isotherms and BJH pore size distribution for HMS-HA-EC (sinter at 650°C)

The assembled and growth of HA into the pores of HMS, could decrease the surface areas of mesoporous materials and also increase the pore size.

3.2 FTIR spectra

The FTIR spectra of HMS-HA and HMS were shown in Fig. 4. The Si–OH vibration band at 960 cm^{-1} in HMS-HA almost disappeared. Therefore, it could be concluded that Si–OH group on the pore wall have been grafted with certain group of hydroxyapatite. Through further research, we found Si–OH might be linked with hydroxyl group of hydroxyapatite. FTIR results of HMS-HA with Si/Ca ratios of 3, 6, and 10 favored our hypothesis: the band at 960 cm^{-1} that corresponds to Si–OH vibration of HMS and the bands at 635 cm^{-1} which was assigned to the stretching mode of hydroxyl group of hydroxyapatite decreased with the Si/Ca ratios increased. And the FTIR spectra of HMS-HA with Si/Ca ratio of 3 exhibited weak intensity at the wave number of 635 and 960 cm^{-1}.

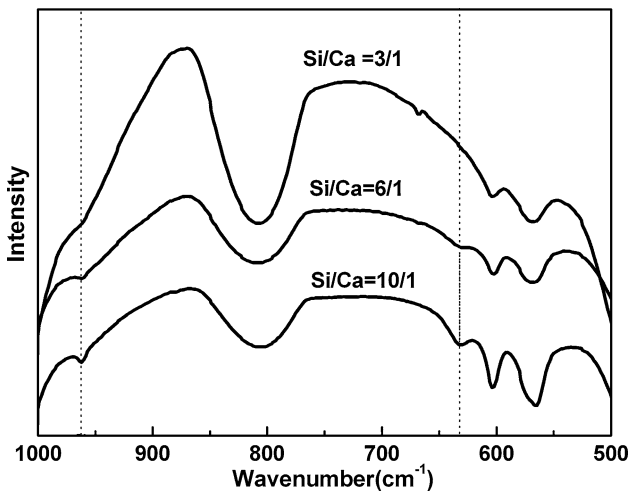

Fig. 4 FTIR spectra for calcined HMS-HA composites with Si/Ca equal 3, 6, and 9

Apatite nucleation in the pores of HMS is a puzzling question. Some researchers posed different mechanisms to explain the bonding between Si and P in apatite and other similar materials. One mechanism called for the calcium ion to adsorb at the silanol site with subsequent attachment of the phosphate ion and form a direct Si–O–P bond at the surface [32, 33]. However, other researchers found the ionic bond lengths of a P–O bond with tetrahedral coordination (0.157 nm) were comparable to a similarly coordinated Si–O bond (0.166 nm). The substitution of a phosphate group (PO_4^{3-}) for a silicate group (SiO_4^{4-}) in a crystal structure would be feasible provided there was charge balance to account for the more negative silicate group. So the presumption we proposed that might explain the structure of HMS-HA. The decrease of the hydroxyl as shown in Fig. 4 possibly indicated a compensation for the extranegative charge of the silicon in the HMS introduced in the HAP structure and replace the phosphorus in the structure of HAP [34, 35].

3.3 Thermal analysis

Figure 5 showed the DTA curves of HMS-HA material which do not resist high temperature process. A sharp endothermic peak at 70–100°C corresponded to a 5% change in weight loss. This change indicated the evaporation of ethanol and deionic water. Several broad endothermic peaks between 200 and 400°C corresponding to a rapid drop in the weight loss curve, indicated DDA decomposition and the mesopores form. When the temperature above 500°C, there was almost no change in TGA curve, which meant DDA was removed thoroughly. A weak exothermic exothermic peak at about 400°C was

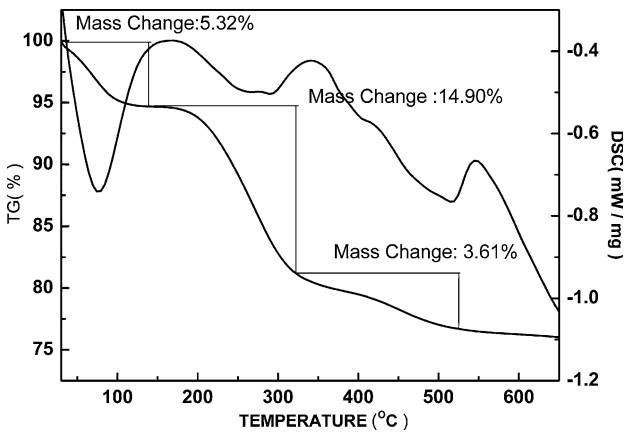

Fig. 5 TGA curves of HMS-HA

observed, which represented the formation of crystalline apatite. A strong endothermic peak appeared at 516°C, corresponding to liberation of CO_2 and the formation of apatite without carbonate.

As one of the common surfactants for chemical products, DDA can cause skin irritations, subacute dermaltitis, and even has some irritable effects on central nerves system. So, DDA may impact on the performance of materials applied in tissue engineering or some other fields on life sciences. However, no evidence has been found about the residues of DDA in the final products from DTA and FTIR spectra.

3.4 Microstructure of HMS-HA

The morphology and structure of the products were investigated by SEM and HRTEM. The SEM images in Fig. 6 demonstrated the surface structure of HMS (a) and HMS-HA (b), both materials kept the irregular sheet-shaped surface morphology. The HRTEM image in Fig. 7a displayed HMS-HA existed many separated hydroxyapatite crystals distributing around the bulky HMS with sheet-shaped surface. It could be found that the separated hydroxyapatite crystals did not combine in the mesoporous silica and the average size of the crystals was less than 50 nm, according to the results of XRD. However, more tiny details could be found in the HRTEM micrograph in Fig. 7b1. From this enlarged image of the area labeled by a rectangle, the well-resolved, continuous parallelism of the lattice fringes with the same orientation belonging to a HA crystal in the mesopores implied that subunits oriented assemble with each other and finally formed a regular structure.

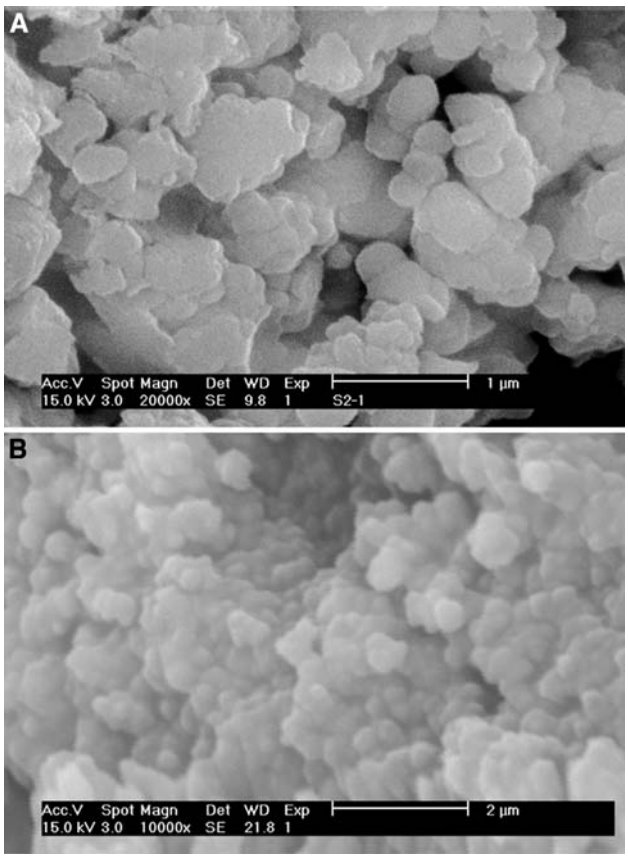

Fig. 6 SEM micrographs of HMS (**A**) and HMS-HA (**B**) materials

A perfect self-assembly for HA in mesoporous materials relied on the specific flat surface of the particles. In general, a plane with close-packed rows of atoms was energetically favored for 3-D crystals according to the periodic bond chain model [31]. HMS possesses erect pores, and the wormhole channel motif base was flat due to a rather quick self-alignment of silicate-encased micelles. Hence, hydroxyapatite crystals facilitated to assemble into the mesopores of HMS. However, some dislocations destroyed the perfect parallel structure. Two main reasons could explain this phenomenon. Unlike the regular hexagonal pores of MCM-41 mesoporous materials, the nonuniformed worm-like pores of HMS impacted on the growth direction of hydroxyapatite crystals. On the other hand, not all the mesopores contain nanoHA crystals, so the dislocations between two regions of uniform structure emerge. The HRTEM image of HMS was shown in Fig. 7b2; HMS did not exhibit the order structure as HMS-HA.

The amorphous apatite assembled into HMS was exhibited in the Fig. 7c. The atomic weight of the elements which belonged to HMS and HA was following the order: Si < P < Ca, and the HRTEM image color of different materials have close relationship with the molecular weight of materials. HA would have darker image color than HMS, because of the heavier atomic weight of Ca and P which would partly block the transmission of electron beam.

3.5 In vitro degradation

Figure 8 showed the mass remaining of HMS-HA-EE and HMS-HA-EC. A noticeable difference in mass remaining between HMS-HA-EE and HMS-HA-EC was observed. The degradation of HMS-HA-EE was fast and its mass lost almost 40% in 60 days; the mass of HMS-HA-EC which sintered at 650°C did not indicate almost any change at 60 days. However, after 60 days, the mass of HMS-HA-EE kept still. This result can be attributed to the hydroxyapatite in HMS-EE had weak or no crystallinity as shown in Fig. 2, thus HMS-HA-EE degraded remarkably compared with HMS-HA-EC which is comprised of well-crystalline HA. The mass loss of HMS-HA-EE nearly consisted with the original mass of Ca^{2+} and PO_4^{3-} in $Ca(NO_3)_2$, $(NH_4)_2HPO_4$, respectively. Herein, the HA with weak or no

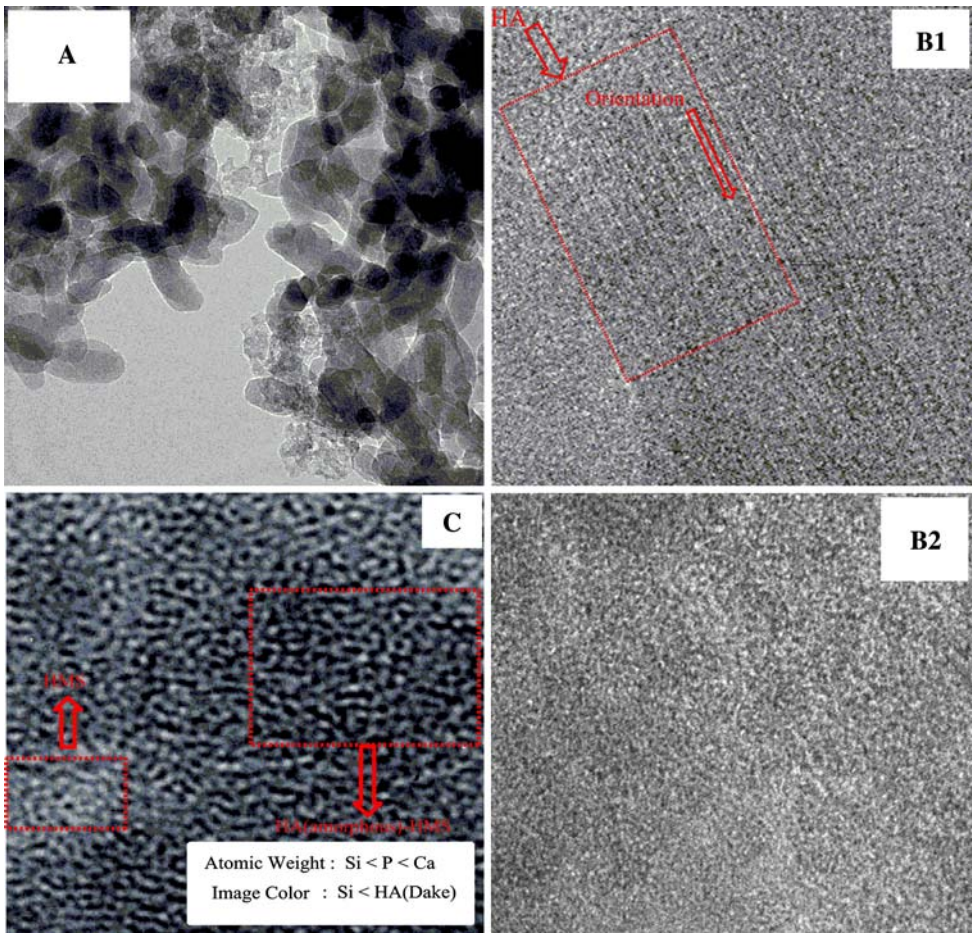

Fig. 7 HRTEM micrographs of HMS-HA-EC materials (sinter at 650°C) (**A**, **B1**), HMS (**B2**) and HMS-HA-EE (**C**)

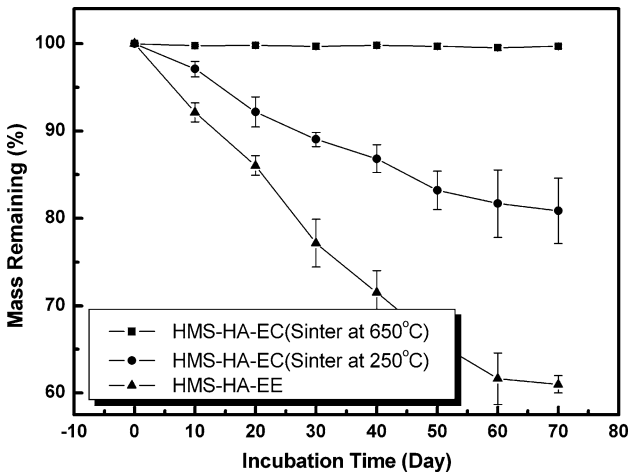

Fig. 8 Mass remaining of HMS-EE and HMS-EC (sinter at 250 and 650°C) in deionised water at 37°C as a function of time (70 days)

crystallinity in the mesopores was entirely dissolved in water. The result of HMS-HA degradation in vitro indicated the crystallinity of hydroxyapatite which can be controlled by changing the sinter temperature.

3.6 The synthesis scheme of HMS-HA mesoporous materials

HMS-HA was synthesized by two methods, and both methods had the similar synthesis scheme (Fig. 9) based on the matured methods of HA and HMS synthesization. An approximate hexagonal structure had been assembled by DDA when it reached a given concentration in the hybrid solution consisting of water and ethanol. When mixing Ca^{2+} and PO_4^{3-} with DDA, the nonuniformed sheet structure was not destroyed.

With the sheet structure of DDA form, TEOS self-assembled in the surface of DDA sheet structure through hydrogen bonding between the electron lone pairs on the nitrogen of the surfactant and the proton on hydroxyl group of the silanol precursor*. At the same time, Ca^{2+} and PO_4^{3-}, which had been involved in TEOS, mutually reacted in appropriate temperature and pH value, and finally formed nanocrystalline hydroxyapatite. The former process of HA accorded with the wet method utilizing to synthesize HA generally. After aging period, template removal and growth

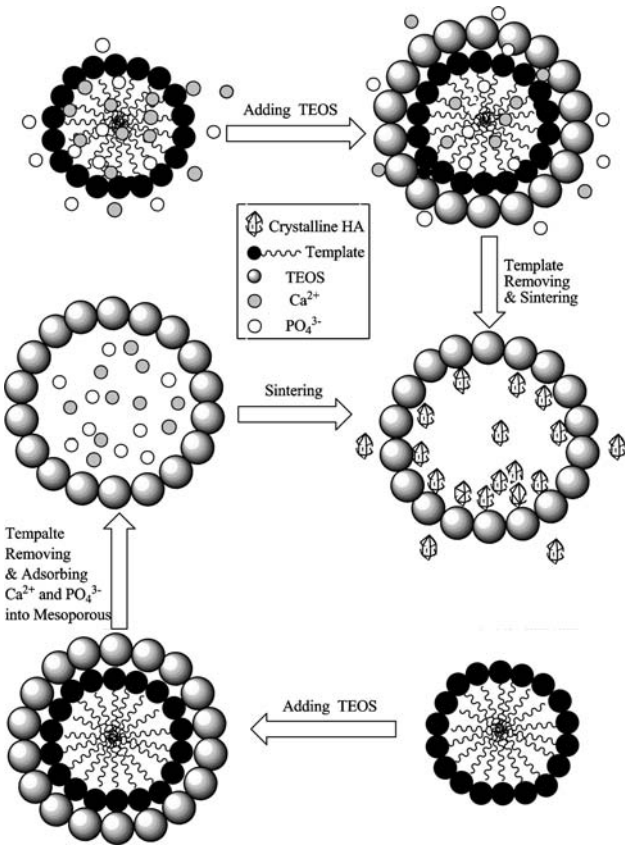

Fig. 9 Schematic illustration of HMS-HA composite

of HA crystals were simultaneous. Template removal produced a mass of silicate hydroxyl exposed on the pore wall of HMS. The relative effect between silicate hydroxyl and the hydroxyl belonged to HA; enabled HA crystals coalesce with mesoporous silica, causing significantly uniform stepwise monolayer. The worm-like mesoporous structure led to epitaxy of HA crystals and the effect of epitaxy oppositely charged pore sizes and shapes of HMS. If Ca^{2+} and PO_4^{3-} were added into the solution containing HMS-HA-EE after template was removed, fewer hydroxyapatite particles was adsorbed into the pores of HMS than that of the method blending HA with DDA in the first step for producing HMS-HA. Hence, the method 2 was a more effective way to fabricate HMS-HA with more HA crystals in the mesopores.

4 Conclusions

A novel HMS-HA hybridized material has been designed in this study. Two independent synthetic methods are adopted and pure HMS-HA composites with controlled different crystallinity of nanoHA are generated in situ in HMS mesopores. The results indicated that the method 2, by which Ca^{2+} and PO_4^{3-} are directly combined with DDA, yields greater HA precipitation in the mesoporous structure. HMS-HA composite material is not a simple blend of HA and HMS, but made by self-assembly of HA crystals in HMS mesopores in situ. HMS-HA, as a new biomaterial consisting of multi-components with bioactivity, biocompatibility and nanoporosity, holds a high potential for biomedical applications.

Acknowledgments This research was supported by the National Basic Research Program of China (Grant 2005CB623902), the National Natural Science Foundation of China (Grant 50572029), the Natural Science Foundation Team Project of Guangdong (Grant 4205786), and the Key Programs of the Ministry of Education (Grant 305012). And we thank Dr. Dong-An Wang at Nanyang Technological University (Singapore) for helpful revision.

References

1. V.D. Khavryuchenko, O.V. Khavryuchenko, V.V. Lisnyak, J. Solid State Chem. **180**, 702 (2007)
2. J.D. Chen, Y.J. Wang, K. Wei, S.H. Zhang, X.T. Shi, Biomaterials **28**, 2275 (2007)
3. E.S. Ahn, N.J. Gleason, A. Nakahira, J.Y. Ying, Nano Lett. **1**, 149 (2001)
4. I. Ono, T. Yamashita, H.Y. Jin, Y. Ito, H. Hamada, Y. Akasaka, M. Nakasu, T. Ogawa, K. Jimbow, Biomaterials **25**, 4709 (2004)
5. Q. Xu, Y. Tanaka, J.T. Czernuszka, Biomaterials **28**, 2687 (2007)
6. E.M. Carlisle, Nutr. Rev. **40**, 210 (1982)
7. E.S. Thian, J. Huang, S.M. Best, Z.H. Barber, W. Bonfield, Mater. Sci. Eng. C **27**, 251 (2007)
8. A.M. Pietak, J.W. Reid, M. Sayer, Biomaterials **26**, 3819 (2005)
9. A.B. Hazar, Ceram. Int. **33**, 687 (2007)
10. P. Siriphannon, Y. Kameshima, A. Yasumori, K. Okada, S. Hayashi, J. Eur. Ceram. Soc. **22**, 511 (2002)
11. M. Regina, T. Filgueiras, G.L. Torre, L.L. Hench, J. Biomed. Mater. Res. **27**, 445 (1993)
12. C. Chan, I. Thompson, P. Robinson, J. Wilson, L. Hench, Int. J. Oral Max. Surg. **31**, 73 (2002)
13. I.D. Xynos, A.J. Edgar, L.D. Buttery, L.L. Hench, J.M. Polak, Biochem. Biophys. Res. Commun. **276**, 461 (2000)
14. P. Handa, M. Stjerndahl, K. Holmberg, Micropor. Mesopor. Mater. **100**, 146 (2007)
15. R. Luque, J.M. Campelo, T.D. Conesa, D. Luna, J.M. Marinas, A.A. Romero, Micropor. Mesopor. Mater. **103**, 333 (2007)
16. M.N. Timofeeva, S.H. Jhung, Y.K. Hwang, D.K. Kim, V.N. Panchenko, M.S. Melgunov, Y.A. Chesalov, J. Chang, Appl. Catal. A. **317**, 1 (2007)
17. Y. Sakamoto, K. Nagata, K. Yogo, K. Yamada, Micropor. Mesopor. Mater. **101**, 303–311 (2007)
18. X. Li, L. Zhang, X. Dong, J. Liang, J. Shi, Micropor. Mesopor. Mater. **102**, 151 (2007)
19. Q. Tang, X. Yao, W. Dong, Y. Sun, J. Wang, X. Jun, D. Feng, J. Control Release **114**, 41 (2006)
20. Z. Wu, Y. Jiang, T. Kim, K. Lee, J. Control Release **119**, 215 (2007)
21. D.R. Radu, C. Lai, K. Jeftinija, E.W. Rowe, S. Jeftinija, V.S. Lin, J. Am. Chem. Soc. **126**, 13216 (2004)
22. A. Corma, Chem. Rev. **97**, 2373 (1997)
23. G.J. Soler-Illia, C. Sanchez, B. Lebeau, J. Patarin, Chem. Rev. **102**, 4093 (2002)
24. T.T. Peter, J.P. Thomas, Chem. Mater. **8**, 2068 (1996)

25. M.P. Ginebra, T. Traykova, J.A. Planell, J.Control Release **113**, 102 (2006)
26. M. Stigter, J. Bezemer, K. de Groot, P. Layrolle, J. Control Release **99**, 127 (2004)
27. W. Xia, J. Chang, J. Control Release **110**, 522 (2006)
28. A.L. Doadrio, E.M. Sousa, J.C. Doadrio, P.J. Perez, I. Izquierdo-Barba, M. Vallet-Regi, J. Control Release **97**, 125 (2004)
29. C.D. Nunes, P.D. Vaz, A.C. Fernandes, P. Ferreira, C.C. Romao, M.J. Calhorda, Eur. J. Pharm. Biopharm. **66**, 357 (2007)
30. J. Andersson, S. Areva, B. Spliethoff, M. Linden, Biomaterials **26**, 6827 (2005)
31. K. Wei, Y.J. Wang, C. Lai, Mater. Lett. **59**, 220 (2005)
32. C.C. Silva, A.S.B. Sombra, J. Phys. Chem. Solids **65**, 1031 (2004)
33. C.L. Yang, W.J. Weng, P.Y. Du, G. Shen, G.R. Hang, Key Eng. Mater. **2**, 330 (2007)
34. I.R. Gibson, S.M. Best, W. Bonfield, J. Biomed. Mater. Res. **44**, 422 (1999)
35. Y. Zhu, W. Zhao, H. Chen, J. Shi, J. Phys. Chem. **111**, 5281 (2007)